Assessment of 3D-RANS models for the simulation of topographically forced shallow flows

Akbar Safarzadeh[1*], Wernher Brevis[2]

[1] Department of Civil Engineering, University of Mohaghegh Ardabili, Daneshgah Street, 56199-11367, Ardabil, Iran.
[2] Structural and Civil Engineering Department, University of Sheffield, Sir Frederick Mappin Building, Mappin Street, Sheffield, S1 3JD, UK.
[*] Corresponding author. E-mail: safarzadeh@uma.ac.ir

Abstract: In this work the performance of Reynolds Averaged Navier-Stokes (RANS) simulations to predict the flow structure developed by the presence of a sidewall obstacle in a uniform open-channel shallow flow is discussed. The tested geometry was selected due to its important role in several fluvial applications, such as the control of riverbank erosion and the creation of improved ecological conditions in river restoration applications. The results are compared against experimental laboratory velocity fields obtained after Large Scale Particle Image Velocimetry (LSPIV) measurements. It is shown that the length of reattachment of the separated shear layer generated by the obstacle is well predicted by a Reynolds Stress Model, while classical two-equation models show important limitations. All the performed RANS simulations are unable to properly predict the formation of a secondary gyre region, which develops immediately downstream the obstacle.

Keywords: Shallow flow; RANS; SPIV; Side obstacle; Shear layer; Turbulence.

INTRODUCTION

Shallow flows can be found in ubiquitous environmental flows such as those occurring in wide rivers and coastal regions. Jirka (2001) defines shallow flows as predominantly horizontal flows in a fluid domain for which the two horizontal dimensions greatly exceed the vertical one. The presence of a limited vertical dimension constrains the vertical evolution of the vortex stretching process, triggering the development of horizontal structures characterised by a highly organized vortical motion, termed quasi two-dimensional coherent structures (2DCS). According to Jirka (2001) the generation mechanism of 2DCS can be classified in three types: Type "A" caused by topographical forcing, Type "B" due to internal transverse shear instabilities and Type "C" produced by secondary instabilities of the vertically sheared base flow.

Type "A" is the most energetic generation mechanism of 2DCS and typically occurs whenever a topographical singularity generates a strong flow separation. Bridge abutments, single groynes and island are just a few examples where topographical forcing can develop. Type "B" occurs as a result of a velocity gradient, which is high enough to produce an unstable velocity field leading to the formation of a train of vortical structures or shear layer. These structures can be found in stream confluences (Rhoads and Sukhodolov, 2004; Uijttewaal and Booij, 2000) at the interface between groyne fields and main flow (Brevis, 2009, Brevis et al., 2014), in harbour entrances, and at the interface of vegetated regions (White and Nepf, 2007).

This work deals with the flow developed downstream a lateral single obstacle. This case was selected due to the simultaneous occurrence of two-generation mechanisms; topographical forcing and internal shear instability. Firstly, the obstacle induces a transverse contraction, which breaks the horizontal symmetry of the approaching flow. Due to the resulting adverse pressure gradient, the main flow separates shedding vortices from the obstacle head. Secondly, and depending on the flow shallowness, the separation gives rise to a main and secondary recirculation cells (Talstra et al., 2006). The lateral flow velocity difference between the recirculating regions and the main flow leads to the development of an intense shear region, resulting in an enhanced growing of the shear layer vortex. Furthermore, and in case of shallow conditions, the bottom friction can constrain the development of the horizontal large-scale structures (Uijttewaal and Booij, 2000). As explained later in the work, due to the shallow conditions selected the physics associated to this flow is particularly complex. Due to the practical importance of the geometrical conditions, which are widely recognized by the engineering community, it is therefore important to measure the reliability of accessible numerical models for its simulation.

Currently several approaches exist for the simulations of turbulent fluid flows. Direct Numerical Simulations (DNS) have become a crucial tool to improve the understanding of fundamental turbulence phenomena such as intermittency (Ishihara et al., 2009) and the dynamic of near wall coherent structures (Adrian and Marusic, 2012). Due to the high computational cost of DNS simulations they are normally constrained to small physical domains and relatively low Reynolds numbers. Advances have been made to develop eddy-resolving techniques such as Large Eddy Simulation (LES) and Detached Eddy Simulations (DES), however they still remain computationally prohibitive for practitioners requiring routine calculations of high Reynolds numbers flows such as those found in nature. Thus it is still necessary to evaluate the performance of statistically based RANS approaches to simulate the time-averaged characteristics of such flows. This work aims at assessing the performance of three RANS turbulent closures for the simulation of the flow developed by the presence of a lateral hydraulic structure in a shallow flow. The paper starts with the theoretical background of the RANS simulation, followed by a description of the experiments performed for the validation of the numerical results and a discussion of the performance of the RANS models in terms of the mean flow characteristics.

RANS EQUATIONS

Following the Reynolds decomposition, the instantaneous velocity can be written as $u_i = u_i' + U_i$, where u_i' and U_i are the fluctuating and mean velocity components, respectively and $i = 1, 2, 3$. Based on this definition and assuming an incompressible fluid flow, the equation of continuity and momentum balance for the mean motion, in Cartesian coordinates, can be written as (Celik and Rodi, 1984):

$$\frac{\partial U_i}{\partial x_i} = 0 \tag{1}$$

$$U_j \frac{\partial U_i}{\partial x_j} = -\frac{\partial P}{\partial x_i} + g_{x_i} + \mu \frac{\partial^2 U_i}{\partial x_i x_j} + \frac{\partial R_{ij}}{\partial x_j} \tag{2}$$

where x_i is the position vector, P is the mean pressure and μ is the dynamic viscosity. $R_{ij} = -\rho\overline{u_i'u_j'}$ is the Reynolds stress tensor, where the sub-index $i, j = 1, 2, 3$. The Reynolds stress can be approximated using the Boussinesq's assumption:

$$-\rho\overline{u_i'u_j'} = 2\mu_t S_{ij} - \frac{2}{3}\rho k \delta_{ij} \tag{3}$$

where, μ_t is the eddy viscosity and S_{ij} and k are the mean strain rate tensor and the turbulent kinetic energy respectively. δ_{ij} is the kronecker delta.

Reynolds stresses can be estimated using several models, however no model is accepted universally for solving the broad range type of problems that can be found in turbulent flows. In this work the $k - \varepsilon$ and $k - \omega$ turbulence models have been selected due to their common use by practitioners, and the RSM models due to its different approach and affordability. The next section summarises the main characteristics of these turbulence models.

STANDARD k-ε TURBULENCE MODEL

The simplest and most widely used RANS turbulence closure is the two-equations $k - \varepsilon$ model, which solves two transport equations to estimate the magnitude of the turbulent kinetic energy, k, and its dissipation rate, ε. According to this model, the eddy viscosity (μ_t) can be related to k and ε, through the expression (Launder and Spalding, 1972):

$$\mu_t = \rho C_\mu \frac{k^2}{\varepsilon} \tag{4}$$

The transport equations for k and ε, can be written as:

$$U_i \frac{\partial k}{\partial x_i} = \frac{\partial}{\partial x_i}\left(\frac{\mu_t}{\rho\delta_k}\frac{\partial k}{\partial x_i}\right) + G - \varepsilon \tag{5}$$

$$U_i \frac{\partial \varepsilon}{\partial x_i} = \frac{\partial}{\partial x_i}\left(\frac{\mu_t}{\rho\delta_\varepsilon}\frac{\partial \varepsilon}{\partial x_i}\right) + c_{\varepsilon 1}\frac{\varepsilon}{k}G - c_{\varepsilon 2}\frac{\varepsilon^2}{k} \tag{6}$$

In the above equations G is the turbulence production by mean shear. The value of the coefficients involved in Equations (8) and (9), and used in this work, is summarized in Table 1.

Table 1. Closure coefficients used for the $k - \varepsilon$ model.

C_μ	$c_{\varepsilon 1}$	$c_{\varepsilon 2}$	δ_k	δ_ε
0.09	1.44	1.92	1.00	1.30

STANDARD k-ω TURBULENCE MODEL

Another widely used two-equation model is the $k - \omega$ model introduced by Wilcox (1994). In contrast to the $k - \varepsilon$ model, the $k - \omega$ model solves the transport equation for the rate of dissipation, i.e. the turbulent frequency ω. Dimensionally ω can be related to by $\omega = \varepsilon/k$ and the eddy viscosity can be related to k and ω through the following equation (Wilcox, 1994):

$$\mu_t = \rho \frac{k}{\omega} \tag{7}$$

The turbulence quantities k and ω are calculated by solving the following transport equations:

$$\rho\frac{\partial k}{\partial x_i} = \frac{\partial}{\partial x_i}\left[\left(\mu + \frac{\mu_t}{\delta_k}\right)\frac{\partial k}{\partial x_i}\right] + \tau_{ij}\frac{\partial U_i}{\partial x_j} \\ -\beta^* \rho k \omega \tag{8}$$

$$\rho\frac{\partial \omega}{\partial x_i} = \frac{\partial}{\partial x_i}\left[\left(\mu + \frac{\mu_t}{\delta_\omega}\right)\frac{\partial k}{\partial x_i}\right] + \alpha\frac{\omega}{k}\tau_{ij}\frac{\partial U_i}{\partial x_j} \\ -\beta\rho\omega^2 \tag{9}$$

where, τ_{ij} is the stress tensor. The coefficients involved in Eqs. 8 and 9, and used in this work, are summarized in Table 2.

Table 2. Closure coefficients used for the $k - \omega$ model.

α	β^*	β	δ_ω	δ_k
0.09	1.44	1.92	0.5	0.5

RSM TURBULENCE MODEL

The Reynolds stress model (RSM) solves the RANS equations by solving seven transport equations for the Reynolds stresses and an extra equation for ε. According to Launder (1989), the RSM can account for the effects of the streamline curvature, vorticity, circulation, and rapid changes in the strain rate in a more efficient way than the two-equation models; however it requires more computational effort and time. Following Launder (1989), the transport equation for this model can be written as Equation (10). The left hand side terms are the local time derivatives and convection term, C_{ij} respectively. The right hand side terms are the turbulent diffusion, $D_{T,ij}$, molecular diffusion, $D_{L,ij}$, stress production, P_{ij}, pressure strain, ϕ_{ij}, dissipation rate, ε_{ij}, and production by system rotation, F_{ij}, respectively.

$$\underbrace{\frac{\partial}{\partial t}\left(\rho\overline{u_i'u_j'}\right)}_{local\ time\ derivatives} + \underbrace{\frac{\partial}{\partial x_k}\left(\rho u_k\overline{u_i'u_j'}\right)}_{c_{ij}}$$

$$= \underbrace{-\frac{\partial}{\partial x_k}\left[\left(\rho\overline{u_i'u_j'u_k'}\right) + \overline{p'\left(\delta_{kj}u_i' + \delta_{ik}u_j'\right)}\right]}_{D_{T,ij}}$$

$$+ \underbrace{\frac{\partial}{\partial x_k}\left[\mu\frac{\partial}{\partial x_k}\left(\overline{u_i'u_j'}\right)\right]}_{D_{L,ij}} \underbrace{-\rho\left(\overline{u_i'u_j'}\frac{\partial u_j}{\partial x_k} + \overline{u_j'u_k'}\frac{\partial u_i}{\partial x_k}\right)}_{P_{ij}}$$

$$+ \underbrace{\overline{p'\left(\frac{\partial u_i'}{\partial x_j} + \frac{\partial u_j'}{\partial x_i}\right)}}_{\phi_{ij}} \underbrace{-2\mu\left(\frac{\partial u_i'}{\partial x_k}\frac{\partial u_j'}{\partial x_k}\right)}_{\varepsilon_{ij}}$$

$$\underbrace{-2\rho\Omega_k\left(\overline{u_j'u_m'}\varepsilon_{ikm} + \overline{u_i'u_m'}\varepsilon_{jkm}\right)}_{F_{ij}} \tag{10}$$

Most of the terms in these transport equations, such as C_{ij}, $D_{L,ij}$ and P_{ij} do not require any modelling and are directly solved. However, $D_{T,ij}$, ϕ_{ij} and ε_{ij} need to be modelled to close the equation system (Gibson and Launder, 1978; Launder, 1989). $D_{T,ij}$ is modelled using a simplified scalar turbulent diffusivity. The pressure-strain term can be calculated using linear or quadratic models. The quadratic model proposed by Speziale et al. (1991), has demonstrated a superior performance in case of basic shear flows. The dissipation rate tensor is modelled using the method proposed by Sarkar and Balakrishnan (1990).

EXPERIMENTATION

The experiment was conducted in a tilting shallow flume located at the research laboratory of the Institute for Hydromechanics (IfH), Karlsruhe Institute of Technology, Karlsruhe, Germany. The flume has a rectangular cross section; an effective length $L_t = 18$ m and a width of $B = 1.82$ m. Fig. 1 shows a schematic representation of the experimental facility and the definition of the most important geometrical parameters. A large constant head tank was used to ensure a steady inflow condition and the discharge was regulated by a computer controlled gate and an inductive magnetic flow meter. A rectangular obstacle of dimension 0.25 m × 0.05 m × 0.05 m was placed at a test section located approximately 12 m downstream the inlet and 6 m upstream the outlet.

The length necessary for the full development of the boundary layer, was estimated based on the relation proposed by Kirkgöz and Ardiclioglu (1997) for a smooth wall. This relation indicated the presence of a fully developed boundary layer at the test section. The height of the obstacle was larger than the selected water depth, H, and it was positioned perpendicular to the direction of the incoming open channel flow. The origin of the coordinate axis was located at the downstream face of the obstacle at the junction point with the sidewall. $X^* = X/L$

and $Y^* = Y/L$ are the dimensionless streamwise and transverse coordinates respectively, where L is the length of the side obstacle. Table 3 summarizes the experimental conditions. The width to depth ratio, $B/H = 46$ which according to Nezu and Rodi (1985) is characterized by the presence of a multi cellular array of secondary currents. The Reynolds, $Re = \frac{U_0 H}{v} = 29680$ and Froude, $Fr = U_0/\sqrt{gh} = 0.29$, numbers are based on the bulk mean velocity, U_0, and correspond to sub-critical turbulent flow condition. Following Babarutsi et al. (1989), the bed friction number of the incoming flow can be defined as $S = fB/2H$, where f is the bed friction coefficient. Genic et al. (2011) reviewed the most common explicit expressions for the estimation of the friction factor in rough and smooth bed conditions. They found that the equation of Zigrang and Sylvester (1982) provides the most accurate value of friction factor, and that the equation proposed by Haaland (1983) is most suitable for hand calculations. In this work the equation of Zigrang and Sylvester (1982) is used for the estimation of the friction factor:

$$\frac{1}{\sqrt{f}} = -2\log\left\{\frac{r'}{3.7} - \frac{5.02}{Re}\log\left[\frac{r'}{3.7} - \frac{5.02}{Re}\log\left(\frac{r'}{3.7} + \frac{13}{Re}\right)\right]\right\}$$

(11)

In the above expression r' is the relative bed roughness.

For the present experimental case the bed friction number was $S = fB/2H = 0.73$ which according to Babarutsi et al. (1989) falls in the classification of shallow condition.

Large Scale Particle Image Velocimetry was used to measure the instantaneous horizontal velocity field. The measurements were conducted using two synchronized CCD cameras working at an acquisition frequency of 37 Hz. The measurements were conducted in 4 consecutive positions, i.e. a total
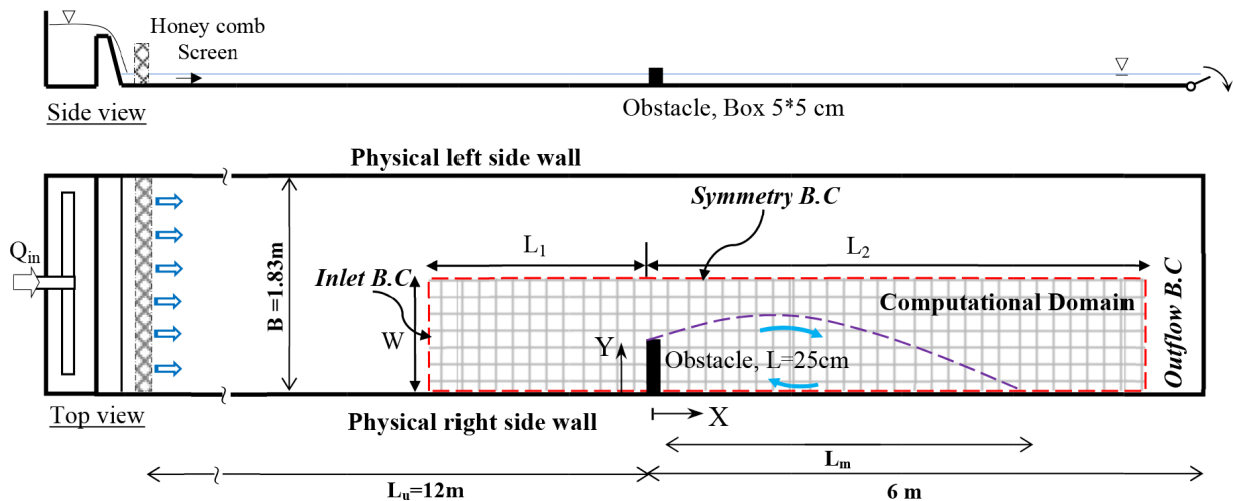

Fig. 1. Schematic representation of the experimental test case. The area denoted by red dashed lines shows the computational domain in the present numerical simulation.

Table 3. A summary of experimental data.

Q_{in} (l/s)	H (cm)	I (degree)	U_0 (cm/s)	B/H	Re	Fr	f	S
13.5	4.0	0.01	18	46	29680	0.29	0.032	0.73

of 8 image planes. The flow field was recorded for 10 minutes resulting in a total of 22200 frames per position. The image sequence was processed with the Particle Image Velocimetry (PIV) package for Linux GPIV, using multi-pass and image deformation techniques (Scarano, 2002). The PIV results have been filtered using the local median filter approach of Westerweel and Scarano (2005) and the iterative filtering algorithm proposed by Brevis et al. (2011). The Delaunay based calibration method described by Brevis and Villalba (2011) was used to transform the results from camera coordinates to real world ones.

NUMERICAL SOLUTION

Fig. 1 shows a schematic view of the domain used for the numerical simulations. The domain is extended up to L_1 upstream the side obstacle and extended L_2 in the downstream direction; the width of the simulation domain is called here W. The commercial finite volume code Fluent was used to simulate the flow field. An inlet velocity boundary condition was implemented at the upstream boundary of the simulation domain and its velocity field and turbulence parameters defined based on the results of an additional simulation of the turbulent flow developed in the straight channel of same dimensions.

Using several numerical simulations it was found that the minimum length of $L_1 = 10L$ is enough to ensure that the side obstacle does not affect the inlet boundary. At the downstream end of the model the outflow boundary condition has been used. At this boundary, the flow often reaches a fully developed state. To ensure that this condition was satisfied at the exit of the simulation domain, it was found that the minimum value of $L_2 = 25L$. A wall boundary condition was implemented to the right side boundary of the simulation domain, while to minimize the computational cost; the left side boundary was simulated using a symmetrical boundary condition. The value of $W = 5L$ was obtained also after several preliminary trials. The top boundary was specified as symmetry condition. At the remaining solid boundaries, i.e. channel bed and periphery of the side obstacle, the wall boundary condition was used. Walls were hydraulically smooth and the no-slip and no-flux conditions were imposed. The implementation of wall boundary conditions in turbulent flows starts with the evaluation of:

$$z^+ = \frac{\Delta z_p}{\upsilon} \sqrt{\frac{\tau_w}{\rho}} \tag{12}$$

where Δz_p is the distance of the near-wall node to the solid surface and τ_w is the wall shear stress.

The distance of the first grid surface off the walls is important and depends on the flow conditions, wall roughness and the turbulence model that is used. The $k - \varepsilon$ model uses the wall function to bridge the solution variables at the near-wall cells and the corresponding quantities on the wall; however the $k - \omega$ model resolves the near wall region (sub-laminar layer region). The first grid surface of the solid boundaries was at $\Delta z_p = 0.001$ m, which ensures that the first grid surface off the wall is located almost everywhere at $z^+ = 1$ and that at least two grid surfaces are located within the laminar sub-layer ($z^+ < 5$).

Roache (1994) suggests a grid convergence index, GCI, to provide a consistent manner in reporting the results of grid convergence studies and provide an error band on the grid

convergence of the solution. In this work, the relative length of the main recirculation zone, $L_m^* = L_m/L$, see Fig. 1, was selected as the objective of the grid converging process. The grid convergence study has been performed for all simulations. Here we present a case with full lateral extension of the domain, $W = 7.3L$. Fig. 2-a shows an overview of the computational mesh. The flow field is computed on three grids and the finer grid set to be double the next coarser grid. Table 4 shows the grid information and the resulting L_m^* computed from the solutions. The results obtained by the GCI method to the $W = 7.3L$ case and the three computational grids showed that the predicted length of the recirculation zone using fine grid do indeed lies in the 95% confidence interval.
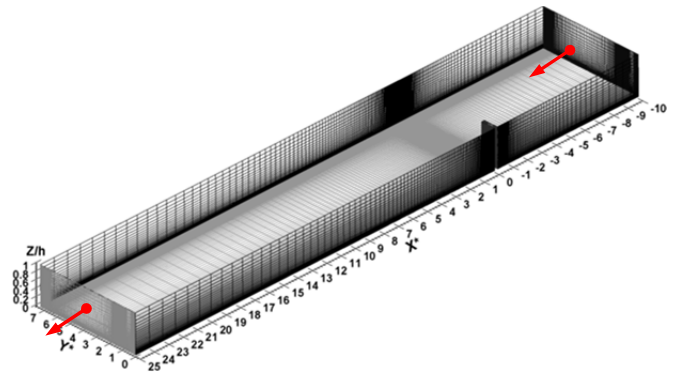

Fig. 2. Computational mesh for simulation with W = 7.3L. The arrow shows the flow direction.

Table 4. Grid information and resulting L_m^* values from numerical simulations.

Mesh code	Number of grid points	Normalized Grid ratio	L_m^*
Coarse	775173	4	10.75
Medium	1550346	2	10.90
Fine	3100692	1	10.94

Due to existence of recirculating and separation regions in the flow field, the convection terms have been discretized using the Second Order Upwind (SOU) scheme (Patankar, 1980). The convergence criterions were set to 10^{-5} for all the residuals of the governing equations to ensure the convergence of the numerical simulation. During the simulation process, the velocity magnitudes at some points have been monitored.

EXPERIMENTAL RESULTS

Fig. 3 and Fig. 5a show the results obtained from the experimental measurements. Fig. 5a shows the presence of a small gyre in the upstream region of the obstacle and two large-scale recirculating regions downstream of it. The larger gyre is developed between $X^* = 3.2$ and $X^* = 11$, and is termed as the downstream primary gyre (DP), the one located between the obstacle and $X^* = 3.2$ is named as the downstream secondary gyre (DS). The reattachment length, L_m, is defined as the distance between the obstacle and the streamline of zero velocity, i.e the quasi-normal streamline to the lateral wall. The value of the reattachment length is approximately 11 times the length of the obstacle.
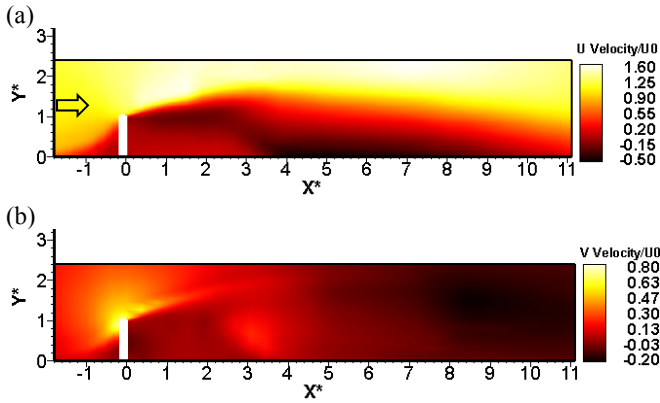
(a)

(b)

Fig. 3. Experimental results. a) Streamwise velocity component, b) Spanwise velocity component.

The length of DS is close to one quarter of the L_m and agrees well with the results reported by Nassiri et al. (2002). A hypothesis for the formation of DS is based on the fact that shallow flow conditions produce an enhanced effect of the bottom roughness on the vertical flow structure, which in this case can decrease importantly the momentum of the current produced towards the upstream region after the impingement of the shear layer. Due to the fact that the flow lack of enough momentum to overcome the local streamwise adverse pressure gradient, arising from the presence of the dead water region at the junction between the downstream face of the obstacle and the side wall, a curvature of the streamlines from the side wall towards the main channel is developed at $X^* = 3.2$. The experimental measurements performed by Safarzadeh (2011) provide support to this hypothesis. Safazadeh (2011) performed experiments for deeper flow conditions for similar geometry finding that only one recirculation region is being formed downstream the obstacle.

Fig. 3 shows the streamwise and spanwise velocity components. As can be seen in the figure the flow in the recirculation region is relatively stagnant compare with the flow in the main channel. Both gyres have similar velocity magnitudes and their maximum streamwise component reach about 50% of the magnitude of the incoming bulk velocity.

Following Castro and Haque (1987) an estimation of the shear layer thickness can be obtained by:

$$\Delta y_H = (y_{0.95} - y_{0.67}) \tag{13}$$

$$\Delta y_L = (y_{0.67} - y_{0.20}) \tag{14}$$

where, Δy_H and Δy_L denotes the high and low boundaries of the shear layer, respectively. y_n is the point at which the velocity is equal to $n\Delta U + U_{min}$, and $\Delta U = U_{max} - U_{min}$ is the total spanwise velocity difference across the shear layer. U_{max} and U_{min} are the maximum and minimum values of the streamwise velocity component, in a particular X^* position.

Fig. 4 shows the inner and outer boundaries of the shear layer obtained from the experimental data using Equations (13) and 14. As observed in the figure an unusual, but dynamically important, change of the shear layer width occurs at $X^* = 3.2$, the interface between DP and DS. A physical explanation for this observation is beyond the scope of this work but a hypothesis, based on the preliminary analysis of the experimental data, not shown here, is that this feature could be the result of a change in the vortex dynamics of the mixing layer caused by the momentum transfer induced by the upstream current.
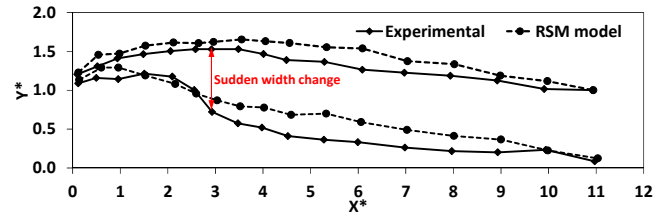

Fig. 4. Comparison of the higher and lower extents of the shear layer calculated for the Experimental and RSM results.

NUMERICAL RESULTS

Figure 5 shows the horizontal streamlines obtained from the numerical results. From a qualitative point of view it is possible to observe that the magnitude of L_m obtained by the two-equation models is shorter than the measured one. In addition it can be noted that the $k - \omega$ model performs better than the $k - \varepsilon$ model. The predicted length by the RSM model is in good agreement with the LSPIV results.

All the performed RANS simulations are unable to properly predict the formation of a secondary gyre region, which develops immediately downstream the obstacle. The lack of precision of the 2-equation models is due to the assumptions of local equilibrium and local isotropy of the eddy viscosity, which is clearly invalid in regions of anisotropic turbulence, such as the separation region.
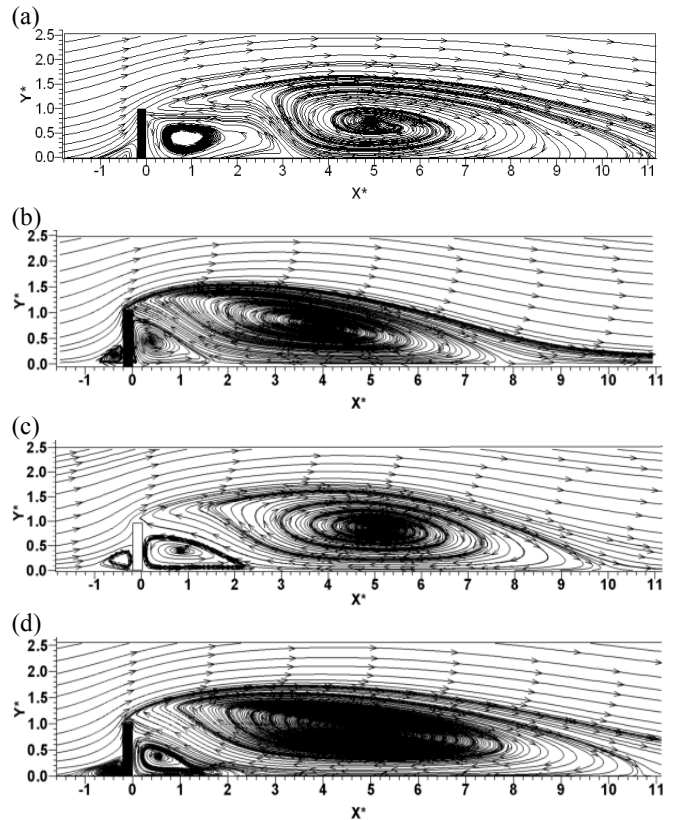
(a)

(b)

(c)

(d)

Fig. 5. Water surface streamlines. a) Experimental, b) $k - \varepsilon$, c) $k - \omega$ and d) RSM models.

Figs. 6a and 6b show more detailed comparisons between the numerical results obtained after the RSM, $k - \omega$ and $k - \varepsilon$ and the experimental measurements. In these figures, RMS re-

fers to root mean square error and is defined as follows:

$$RMS = \sqrt{\sum_{i=1}^{n} (x_n - x_e)^2/n} \qquad (15)$$

where n is the total number of data in each of the individual profiles, x_n and x_e are the numerical and experimental results respectively. In general the critical points for all numerical models are the zones around the obstacles and the interface between the gyres. If the streamwise velocity component is considered, the RSM shows a better performance in the region upstream the obstacle and downstream $X^* = 5$. Immediately downstream the obstacle the performance of the RSM is lower than the other two models (see rectangular region in Fig. 6a). The shear layer region and the zone close to the wall between $X^* = 2$ and $X^* = 2.5$ (See Fig. 6b) is where most of the errors in the streamwise velocity components are located (See Fig. 6c and 6d). Experimental unsteady velocity field showed the presence of coherent vortical structures in that zone.

In downstream positions, $X^* = 8$ and $X^* = 11$ the large scale eddies are dissipated and the flow is characterized by an increased presence of small-scale three-dimensional flow structure, consequently the experimental and RSM results agrees well in that region. As shown in the Fig. 4, and even though L_m is well predicted, the RSM model cannot predict the expansion of the shear layer observed in the experimental results at the gyres interface. Fig. 7 shows a comparison of the turbulent kinetic energy and Reynolds shear stresses between the experiments and RMS results. The main differences show that the Reynolds shear stresses in the shear layer zone immediately downstream the obstacle cannot be properly described, especially in the zone adjacent to the gyres interface. This zone is where the vorticity magnitude increase in thickness, and where a strong increase of the Reynolds shear stresses can be also observed. It is also important to notice the lack of precision in the far wake region, especially in the turbulent kinetic energy magnitudes. This result shows the complex nature of the flow and indicates the need for eddy resolving techniques to properly describe the physics at the interfacial region.
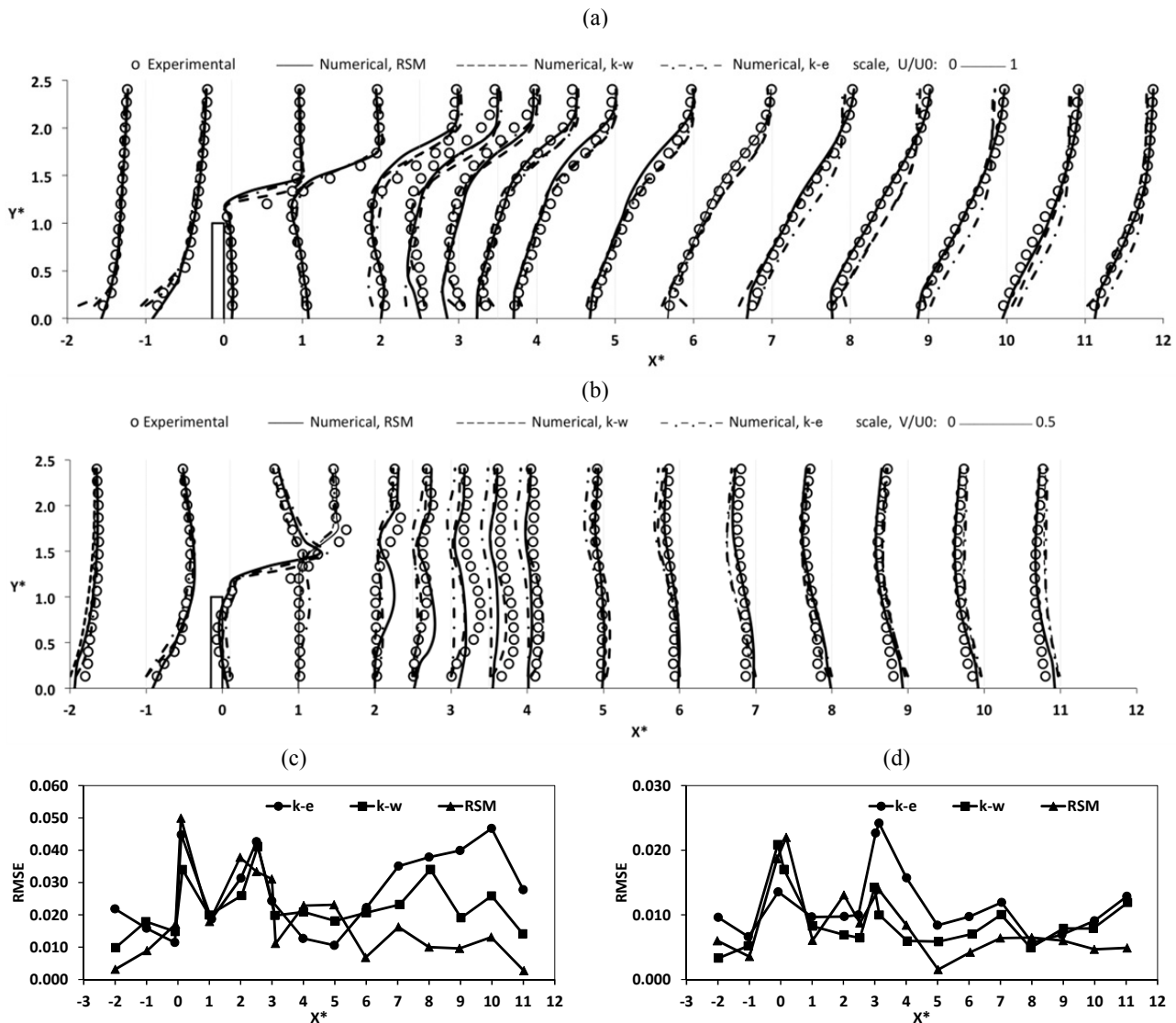

Fig. 6. Comparison between numerical and experimental results. a) Streamwise velocity component, b) Spanwise velocity component, c) Root Mean Square, RMS, between the numerical and experimental streamwise velocity component, d) Root Mean Square (RMS) between the numerical and experimental spanwise velocity component.
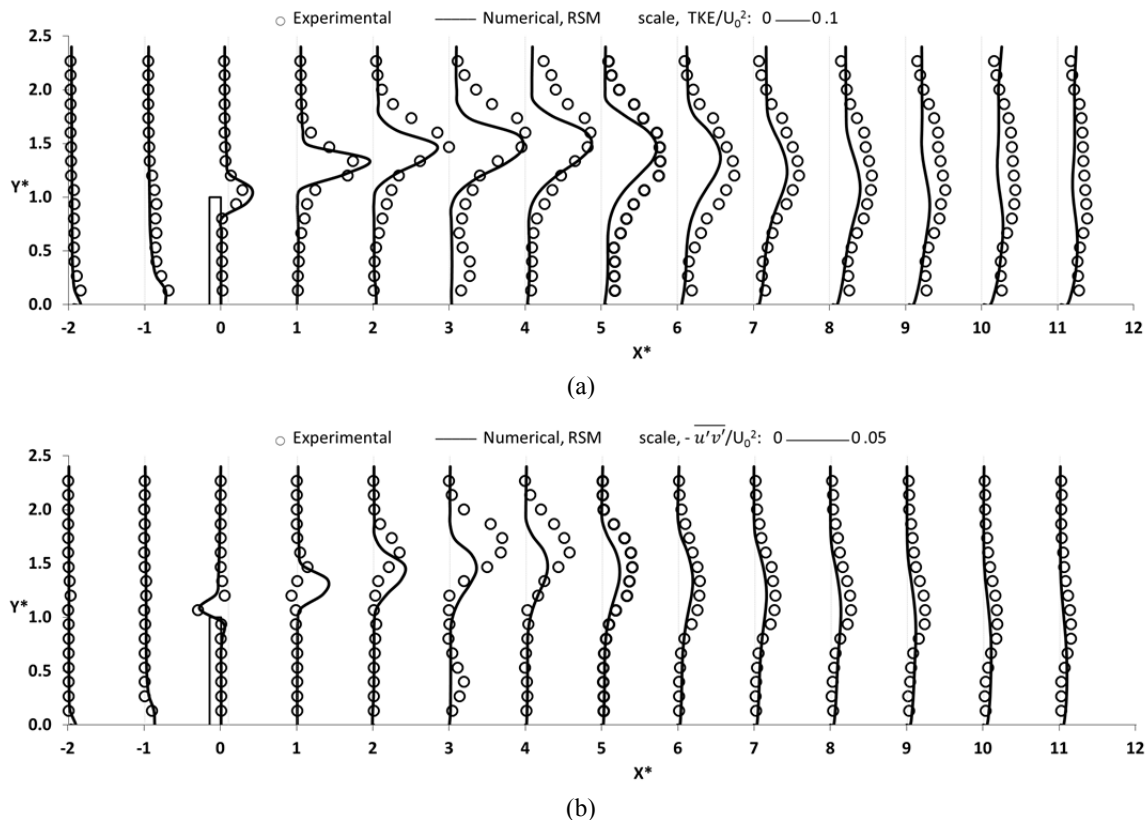
(a)

(b)

Fig. 7. Comparison of turbulence statistics between measurement and RSM model. a) Turbulent Kinetic Energy and b) Horizontal Reynolds stresses.

SUMMARY AND CONCLUSION

An experimental study was conducted to measure turbulent flow around a single side obstacle in a shallow flow using surface Particle Image Velocimetry (SPIV) method. Then a commercial CFD code was used for the prediction of the flow patterns. Three turbulence closure models were employed and the performance of each model was evaluated using experimental data. It was found that the length of the main recirculation region obtained by two-equation models is under-predicted, while the results of the RSM model are in good agreement. All the performed RANS simulations are unable to predict properly the secondary separation region and the lateral expansion of the associated shear layer. The deficiencies of RANS models are attributed to the anisotropy of the coherent structures developed at the shear layer region.

REFERENCES

Adrian, R.J, Marusic, I., 2012. Coherent structures in flow over hydraulic engineering surfaces. Journal of Hydraulic Research, 50, 5, 451–464.

Babarutsi, S., Ganoulis, J, Chu, V.H., 1989. Experimental investigation of shallow recirculating flows. Journal of Hydraulic Engineering, 115, 7, 906–924.

Brevis, W., 2009. Experimental investigation of the flow hydrodynamics in open channel dead regions. PhD thesis, Universidad de Chile, Santiago.

Brevis, W., Niño, Y., Jirka, G.H., 2011. Integrating cross-correlation and relaxation algorithms for particle tracking velocimetry. Experiments in Fluids, 50, 1, 135–147.

Brevis, W., Garcia-Villalba, M., 2011. Shallow-flow visualization analysis by proper orthogonal decomposition. Journal of Hydraulic Research, 49, 5, 586–594.

Brevis, W., Garcia-Villalba, M., Niño, Y., 2014. Experimental and large eddy simulation study of the flow developed by a sequence of lateral obstacles. Environmental Fluid Mechanics, 14, 4, 873–893.

Castro, I.P., Haque, A., 1987. The structure of a turbulent shear layer bounding a separation zone. Journal of Fluid Mechanics, 179, 2, 439–468.

Celik, I., Rodi, W., 1984. Simulation of free-surface effects in turbulent channel flows. Physicochemical Hydrodynamics, 5, 3, 217–227.

Genic, S., Arandjelović, I., Kolendić, P., Jarić, M., Budimir, N., Genić, V., 2011. A review of explicit approximations of Colebrook's equation. FME Transactions, 39, 2, 67–71.

Gibson, M.M., Launder, B.E., 1978. Ground effects on pressure fluctuations in the atmospheric boundary layer. Journal of Fluid Mechanics, 86, 491–511.

Haaland, S.E., 1983. Simple and explicit formulas for the friction factor in turbulent pipe flow. Journal of Fluid Engineering, 105, 1, 89–90.

Ishihara, T., Gotoh, T., Kaneda, Y., 2009. Study of high-Reynolds number isotropic turbulence by direct numerical simulation. Annual Review in Fluid Mechanics, 41, 165–180.

Jirka, G.H., 2001. Large scale flow structures and mixing processes in shallow flows. Journal of Hydraulic Research, 39, 6, 567–573.

Kirkgöz, M.S., Ardiclioglu, M., 1997. Velocity profiles of developing and developed open channel flow. Journal of Hydraulic Engineering, 123, 12, 1099–1105.

Launder, B.E., 1989. Second-moment closure and its use in modeling turbulent industrial flows. International Journal of Numerical Methods in Fluids, 9, 963–985.

Launder, B.E., Spalding, D.B., 1972. Lectures in mathematical models of turbulence. Academia Press, London, England.

Nassiri, M., Chu, V.H., Babarutsi, S., 2002. Simulation of horizontal turbulence in shallow recirculating flows. In: Proc. of 15th ASCE Engineering Mechanics Conference. Columbia University, New York, NY.

Nezu, I., Rodi, W., 1985. Experimental study on secondary currents in open channel flow. In: Proc. of 21st IAHR Congress, Melbourne, Australia, 2, pp. 114–119.

Patankar, S.V., 1980. Numerical Heat Transfer and Fluid Flow. McGraw-Hill, New York.

Rhoads, B.L, Sukhodolov, A.N., 2004. Spatial and temporal structure of a shear layer turbulence at a stream confluence. Water Resources Research, 40, W06304, doi: 10.1029/2003WR002811.

Roache, P.J., 1994. Quantification of uncertainty in computational fluids Dynamics. Annual Review in Fluid Mechanics, 29, 123–160.

Safarzadeh, A., 2011. Experimental study of turbulent flow pattern around a groyne with various head shapes. PhD thesis. Tarbiat Modares University, Tehran, Iran.

Sarkar, S., Balakrishnan, L., 1990. Application of a Reynolds-stress turbulence model to the compressible shear layer. ICASE Report 90-18-NASA CR182002.

Scarano, F., 2002. Iterative image deformation methods in PIV. Measurement Science and Technology, 13, 1, 1–19.

Speziale, C.G., Sarkar, S., Gatski, T., 1991. Modelling the pressure strain correlation of turbulence: an invariant dynamical systems approach. Journal of Fluid Mechanics, 227, 245–272.

Talstra, H., Uijttewaal, W.S.J., Stelling, G.S., 2006. Emergence of large scale coherent structures in a shallow separating flow. In: Proc. Int. Conf. Fluvial Hydraulics (River Flow), Taylor and Francis, U.K., pp. 261–269.

Uijtewaal, W.S.J., Booij, R., 2000. Effects of shallowness on the development of free-surface mixing layers. Physics of Fluids, 12, 2, 392–420.

Westerweel, J., Scarano, F., 2005. Universal outlier detection for PIV data. Experiments in Fluids, 39, 6, 1096–1100.

White, B., Nepf, H., 2007. Shear instability and coherent structures in a flow adjacent to a porous layer. Journal of Fluid Mechanics, 593, 1–32.

Wilcox, D.C., 1994. Simulation of transition with a two-equation turbulence model. AIAA Journal, 32, 2, 247–255.

Zigrang, D.J., Sylvester, N.D., 1982. Explicit approximations to the Colebrook's friction factor. AIChE Journal, 28, 3, 514–515.